The International Journal of Advanced Manufacturing Technology (2018) 96:2443–2453
https://doi.org/10.1007/s00170-018-1801-8

ORIGINAL ARTICLE

Application of high-angle helical-grooved vitrified wheels to cylindrical plunge grinding

S. Dewar[1] · R. Bauer[1] · A. Warkentin[1]

Received: 28 November 2017 / Accepted: 12 February 2018 / Published online: 23 February 2018

Abstract
Cylindrical plunge grinding experiments were carried out to compare the performance of non-grooved and grooved vitrified grinding wheels. The grooved wheels featured high-angle helical grooves with a 50% groove factor. Grinding forces, spindle power, workpiece roundness, and workpiece surface roughness were measured for five different infeed rates. It was observed that, for the conditions used in this research, the grooved grinding wheel reduced the resulting normal forces by 36%, tangential forces by 32%, spindle power by 29%, and specific energy by 28%, while increasing the workpiece surface roughness by 38%. The spark-in and spark-out time constants associated with the grooved grinding wheel were determined by analyzing the normal force data and found to be, on average, 21% lower than the non-grooved grinding wheel. The spark-in and spark-out time constants were also identified and used in a grinding force and infeed model to simulate the plunge grinding process. These simulations showed that, due to the combination of reduced forces and time constants when using a grooved wheel, improvements in overall plunge cycle time of up to 30% could be achievable.

Keywords Grooved · Cylindrical plunge grinding · Vitrified wheels · High helix-angle

1 Introduction

Cylindrical plunge grinding is the most common type of grinding operation [1]. It is used to create high-precision cylindrical features on automotive, aerospace, and marine parts such as cam, crank, and propeller shafts. Given that surface quality tolerance requirements are becoming more stringent and the required surfaces are often created on long slender shafts, it is important that process forces and power be minimized. Furthermore, there is growing concern on the environmental impact of manufacturing; therefore, it is critical that means be found to grind cylindrical parts as efficiently as possible. One potential method to achieve these goals in cylindrical grinding may be to modify grinding wheels with grooves or other patterns since this approach has worked well in flat surface grinding to reduce forces, power, and coolant requirements [2, 3].

✉ R. Bauer
robert.bauer@dal.ca

[1] Department of Mechanical Engineering, Dalhousie University|, Halifax, NS, Canada

These grooves and textures have been applied to a wide range of grinding wheel materials [2]. The present work concentrates on vitrified-bond grinding wheels as they are the most commonly used type of wheel and are economical for many precision grinding applications. Furthermore, they can be grooved on the shop floor or in the lab, making them ideal for changing production or research requirements. According to Forbrigger et al. [3], 25 research papers relating to grinding with grooved vitrified grinding wheels have been published. The first research paper on grooved grinding wheels was in 1977 by Nakayama et al. [4]. To characterize grooved wheels, Verkerk [5] introduced the groove factor η_g which is the ratio of the un-grooved wheel surface to the entire wheel surface. Forbrigger et al. [3] defined a groove on a wheel by its helix angle α_g, groove width b_g, groove depth a_g, and number of grooves N_g as shown in Fig. 1. Only three papers have, to date, focused on cylindrical grinding with grooved vitrified wheels. In 2010, de Oliveira et al. [6] and later da Silva et al. [7] used an electromagnetically actuated single-point diamond shaker to engrave a variety of shallow patterns (0.002–0.025 mm) onto aluminum oxide (Al_2O_3) grinding wheels including four grooves with a low helix angle (angle not reported). Then, they ground steel cylindrical workpieces using integer speed ratios with the objective of creating a variety of patterns on the

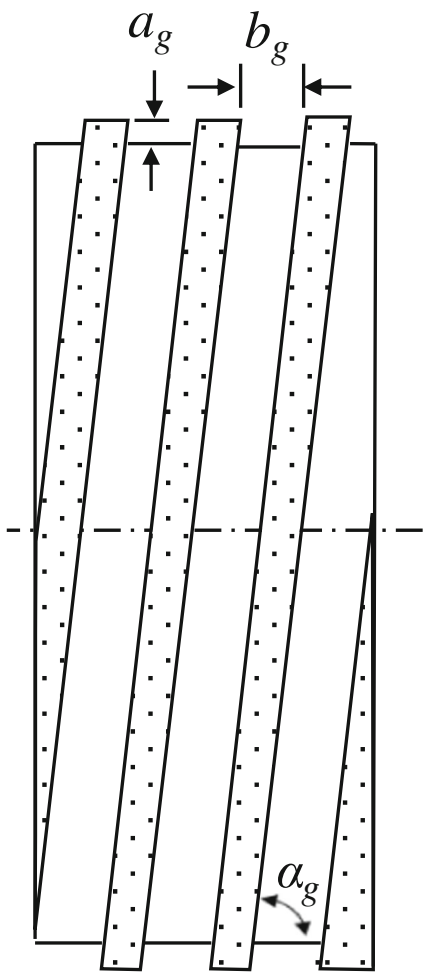

Fig. 1 Geometry of grooved wheels

steel workpieces. They found that grinding power was reduced for all the patterns that they tested. Uhlmann and Hochschild [8] cylindrically ground steel workpieces with vitrified CBN wheels that had 70 deep grooves (5 mm) of various widths (1–5 mm) having a moderate helix angle (32°) and found that grinding forces, power, and temperature decreased while surface roughness and wheel wear increased. In addition, Uhlmann and Hochschild indicated that higher helix angles reduced the dynamic forces associated with grooves entering and exiting the grinding zone.

Mohamed et al. [9] showed that, for flat creepfeed grinding of steel workpieces, a shallow (0.2 mm) single, very high angle (89.7°) groove carved into an aluminum oxide wheel with a single-point diamond could decrease process forces and power by at least 30% and reduce wheel wear. Given that a high-angle helical-grooved vitrified-bond aluminum-oxide wheel has not been studied in the literature for cylindrical grinding, the present paper investigates the use of this grooved wheel in cylindrical plunge grinding to determine its effect on process forces, power, and surface roughness. In addition, the effect of grooves on the time constants in cylindrical plunge grinding will be reported for the first time, and simulations will be performed to determine the potential reduction in total cycle time.

2 Experimental setup

Assessing the effectiveness of a grinding wheel requires that forces be measured which is more complicated in cylindrical grinding than in flat surface grinding due to the rotating workpiece. In this research, an apparatus similar to the setups used by Choi et al. [10] and Drew et al. [11] was developed. The cylindrical plunge grinding experiments were performed on a Blohm Planomat 408 creep-feed grinding machine outfitted with a custom rotary axis (shown in Fig. 2) which enables the measurement of grinding forces. This rotary axis consists of a Suburban Tools Inc. Collet Master 5C collet fixture which is attached via a timing belt to a Kelling 2.47 Nm brushed DC motor and mounted on a Kistler 9257B three-component force dynamometer with a 5019A charge amplifier. This unique apparatus enabled high-precision three-component measurements of cylindrical grinding forces over a wide bandwidth. Grinding power was measured through a Load Controls Inc. PH-3A power transducer. The grinding forces and spindle power were then collected through a National Instruments BNC-2120 connector block connected to a PCI-MIO-16XE-10 data acquisition card. The sampling rate for the data collection was 2500 Hz.

The mean surface roughness R_a of the workpieces was measured using a Mahr Fedral Inc. Pocket Surf. Five randomly spaced surface roughness measurements were taken per workpiece. Workpiece roundness was then measured at the center of each workpiece using a Mitutoyo dial indicator having an accuracy of ± 0.0001 in. (± 2.54 μm).

The workpiece samples used were 25.4-mm diameter precision-ground AISI 1045 steel bar cut to 114.3 mm lengths with an initial roundness of ± 0.001 in. (± 25.4 μm). The samples were ground using a Radiac WRA60-J5-W vitrified aluminum oxide wheel. CIMTECH 310 with InSol was used as a lubricant and it was applied via a coherent jet at a rate of 37.9 lpm. Table 1 summarizes the grinding parameters used.

The experiments consisted of a plunge grinding operation performed at the infeed rates and depths of cut described in Table 2 for both the non-grooved and grooved-wheel cases. The depths of cut were chosen to ensure that the grinding forces reached a steady-state while not causing excessive wheel wear.

The goal of these experiments was to compare the performance of grooved and non-grooved grinding wheels. The non-grooved wheel was dressed with a single-point diamond dresser using an overlap ratio of 7.5. To create the grooved wheel, the grinding wheel was dressed (using the same method as the non-grooved wheel) and then grooved using the

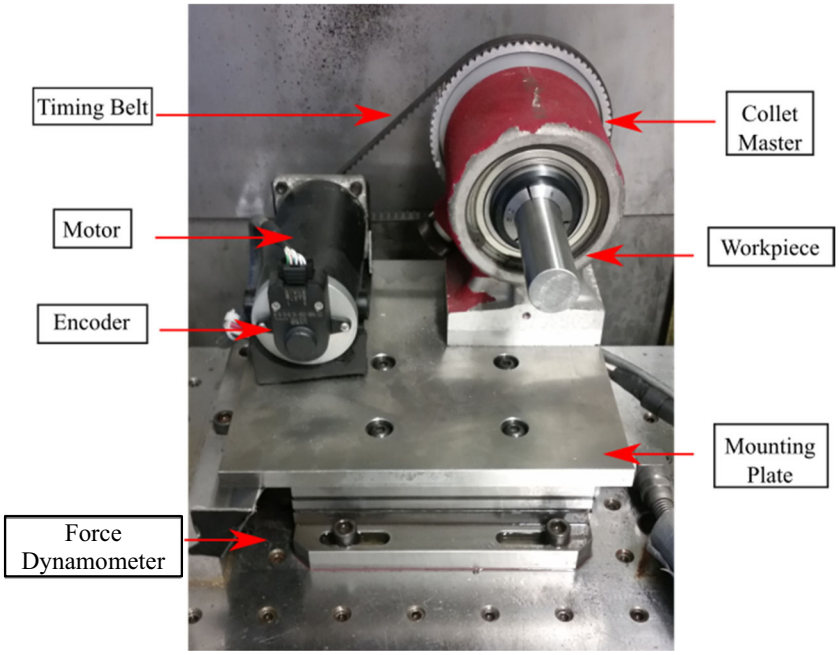

Fig. 2 Rotary axis (without waterproof enclosure)

novel single-point diamond grooving system described by Mohamed et al. [12]. This unique grooving system monitors the spindle encoder and can synchronize the motion of the grinding wheel with the motion of the single-point diamond as it moves across the wheel's surface. This feature enables a wheel to be re-grooved to increase the groove depth or refresh a worn groove geometry. The groove pattern chosen for the present research was a high-angle helical groove with a 50% groove factor as described in Table 3 because this pattern was found to provide the most significant reduction in forces in flat surface grinding studies by Mohamed et al. [13].

Table 1 Grinding parameters used for the cylindrical plunge-grinding experiments

Grinding parameters	Imperial	Metric
Wheel	WRA60-J5-W Radiac	
Wheel material	Aluminum oxide	
Wheel grit	60	
Wheel width	1.05 in	26.7 mm
Wheel diameter	15.6 in	396.2 mm
Wheel speed	979 rpm	
Workpiece material	Precision Ground AISI 1045	
Workpiece diameter	1 in	25.4 mm
Workpiece speed	300 rpm	
Spark-out time	10 s	
Lubricant used	CIMTECH 310 with InSol	
Lubricant concentration	3% Brix	
Lubricant flowrate	10 gpm	37.9 lpm

To ensure repeatability of the experiments, plunge grinding operations were performed twice with both grooved and non-grooved wheels at each infeed rate.

3 Results

Figure 3 plots a sample of the raw normal force data captured using the rotary axis as a function of time. A finite impulse response (FIR) low-pass filter with a passband frequency of 2.5 Hz and a stopband frequency of 6.25 Hz were applied to the raw data to provide a more visible trend. The shape of the filtered results clearly shows three different phases during a plunge grinding operation. Malkin [14] refers to these phases as the initial spark-in, steady-state, and final spark-out phase. During the initial spark-in phase, the grinding wheel is continuously fed into the workpiece at a commanded infeed rate. The resulting grinding forces cause the cylindrical workpiece and the rest of the grinding system to elastically deflect causing the actual infeed to be less than the commanded infeed. The steady-state portion of the curve corresponds to the maximum constant forces and power experienced during the plunge grinding cycle. During this phase, both the elastic

Table 2 Infeed rates and respective depths of cut used in the experiments

Infeed rate μm/rev	Depth of cut μm
1.02	36
2.03	71
3.05	107
4.06	142
5.08	178

Table 3 Groove parameters used in the experiments

Groove parameter	Value	Units
Groove factor η	50%	–
Groove width *bg*	884	μm
Groove depth *ag*	102	μm
Lead *L*	1768	μm/rev
Helix angle	90°	–

deflections and the actual infeed rate are constant. Once the desired commanded depth has been achieved, the grinding wheel's commanded infeed rate is zero and the spark-out phase commences during which time the elastic deflections that accumulated during the spark-in phase are recovered.

The filtered steady-state normal force, tangential force, and spindle power data were averaged over the repeatability experiments and plotted as a function of infeed rate for both the non-grooved and grooved wheels in Fig. 4a–c. Best-fit straight lines were then superimposed on these plots to illustrate the trends observed in the data. The corresponding error bars represent ± 1 standard deviation of the data from the linear fit. The results clearly show an increase in the steady-state normal force, tangential force, and spindle power with increasing infeed rate for both non-grooved and groove wheels. There is, however, a significant reduction in the grinding forces and power across all infeed rates tested when using the grooved grinding wheel. Compared with a non-grooved wheel, the grooved grinding wheel decreased normal forces by an average of 36%, decreased tangential forces by an average of 32%, and decreased spindle power by an average of 29%.

The resulting ground samples were tested for roundness and surface roughness. Roundness measurements showed a consistent 7.6 μm throughout all ground samples, with no

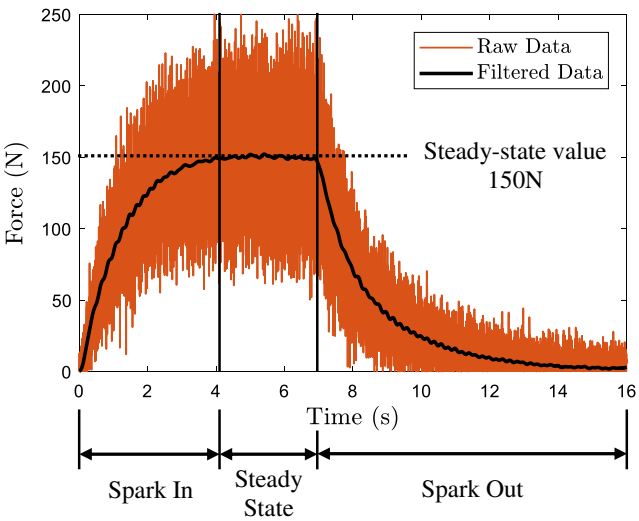

Fig. 3 Raw and filtered force data showing three phases of the plunge grinding operation

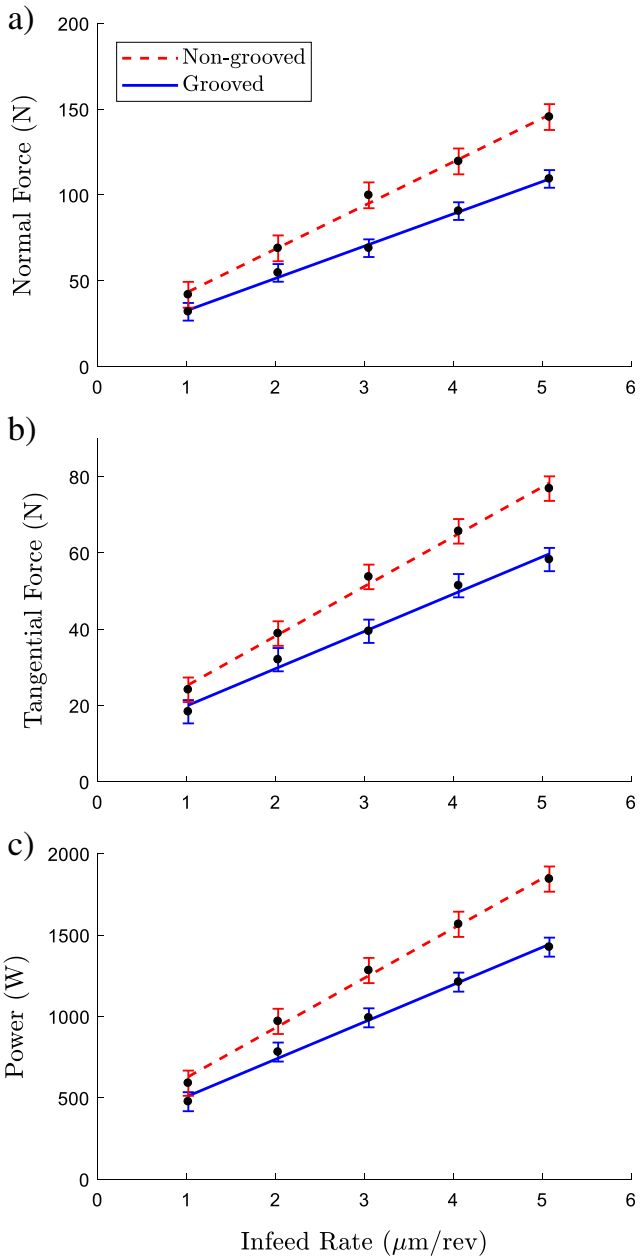

Fig. 4 Normal force, tangential force, and spindle Power vs. infeed rate for cylindrical plunge grinding with grooved and non-grooved wheels

measurable difference between using non-grooved and grooved wheels. The resulting workpiece surface roughness was then averaged over the repeatability experiments and plotted as a function of infeed rate in Fig. 5 for both the non-grooved and grooved wheels. A straight-line curve fit, and corresponding error bars were superimposed on the figure. It can be seen from Fig. 5 that the surface roughness for the samples ground using the grooved wheel showed a slight increase in roughness with increasing infeed rate, while the roughness of samples ground using the non-grooved wheel showed a slight decrease in roughness with increasing infeed rate. Although the grooved wheel resulted in a workpiece

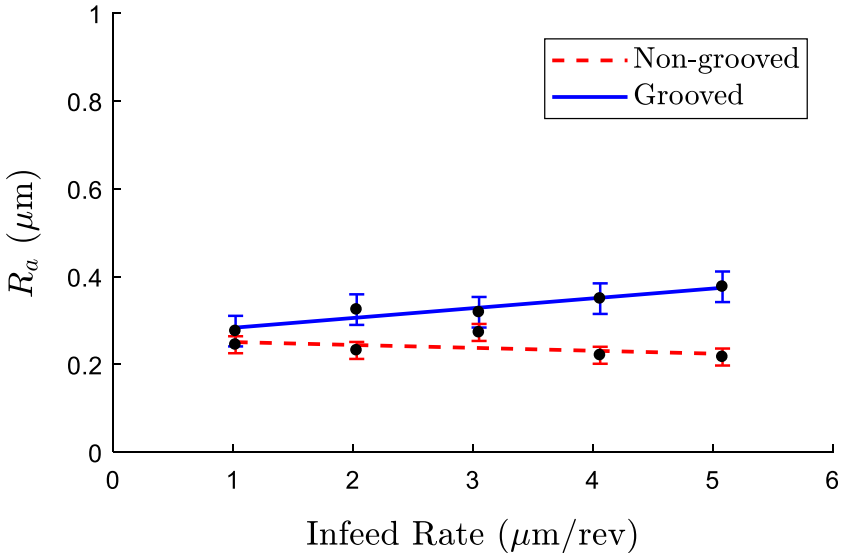

Fig. 5 Workpiece surface roughness vs. infeed rate for cylindrical plunge grinding with grooved and non-grooved wheels

surface roughness that was, on average, 38% higher than the non-grooved wheel, the maximum measured surface roughness in Fig. 5 of about 0.4 μm is well within the 0.1 to 1.6 μm average application range for grinding [15].

4 Analysis

To further compare the performance of non-grooved and grooved grinding wheels for cylindrical plunge grinding, the specific energy, material removal rate, and time constants were examined.

4.1 Specific energy

To highlight the improved efficiency of grooved wheels, the specific energy u of the grinding operation can be derived from the spindle power P_s using the following equation:

$$u = \frac{P_s}{a \cdot b_w \cdot v_w} \tag{1}$$

where a is the depth of cut in mm, b_w is the width of material ground in mm, and v_w is the workpiece speed in mm/s. Figure 6 plots the calculated average specific energy as a function of infeed rate for both the non-grooved and grooved grinding wheels. A second-order polynomial curve fit and corresponding error bars were superimposed on the figure. The grooved wheel had an average reduction of 28% across all infeed rates suggesting that the grooved grinding wheel results in more efficient grinding compared to the non-grooved wheel. A decrease in specific energy was also observed by Mohamed et al. [13] for flat surface grinding using a grooved wheel. Mohamed et al. provided evidence that these efficiency improvements were due to enhanced cutting mechanics because of the large chips removed by the cutting edges on the rims of the grooves (effectively increasing the uncut chip thickness) as well as the enhanced coolant flow through the grinding zone, which could also explain the observed improvements to the forces and power observed in Fig. 4. Furthermore, with the increased uncut chip thickness creating larger cuts into the workpiece, one would anticipate a reduction in surface finish quality as observed in Fig. 5 which is consistent with what has been observed with flat grinding [13].

4.2 Material removal rate

Figure 7 and Fig. 8 plot the resulting material removal rate (MRR) versus the normal force and spindle power, respectively. The average force and power across the repeatability experiments were plotted along with the straight-line curve fit and corresponding error bars for both the non-grooved and grooved wheels. These figures show that grooved wheels can remove much more material for a given normal force or spindle power than non-grooved wheels. Specifically, there is an average 43% increase in MRR for a given normal force and an average 44% increase in MRR for a given spindle power.

4.3 Time constants

While most of the material removal occurs during the spark-in and steady-state phases (called the roughing stage [16]), the spark-out phase can account for a significant percentage of the time it takes to complete a plunge grinding cycle due to long characteristic time constants [16]. Jiang et al. [17] proposed using acoustic emission signals to estimate the time constants during the dwell or spark-out period. In the present work, the measured normal force curves were used to determine the

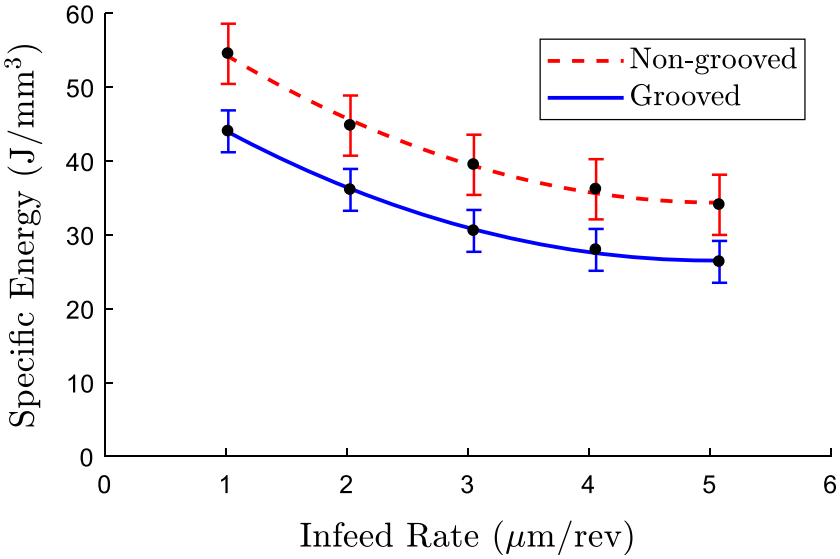

Fig. 6 Specific energy vs. infeed rate for cylindrical plunge grinding with grooved and non-grooved wheels

characteristic time constants of the cylindrical plunge grinding process. For example, Fig. 9 compares the normal force curves for the same grinding operation using a grooved and non-grooved wheel. It can be seen in Fig. 9 that, during spark-in, the grooved wheel curve reaches steady-state more than 1 s faster than the non-grooved wheel curve—meaning faster material removal. Similarly, the spark-out phase for the grooved wheel is about 2.5 s faster than the non-grooved wheel.

To better quantify the improvements of the grooved grinding wheel, the normal force during the spark-in phase F_N^{in} and spark-out phase F_N^{out} were modeled using the following equations:

$$F_N^{in}(t) = F_N^{ss}\left(1-e^{-\frac{t}{\tau^{in}}}\right) \quad (2)$$

$$F_N^{out}(t) = F_N^{ss}\, e^{-\frac{t}{\tau^{out}}} \quad (3)$$

where F_N^{ss} is the steady-state normal force, t is the time, and τ^{in} and τ^{out} are the spark-in and spark-out time constants. The spark-in and spark-out normal force curves were fitted using Matlab's exponential fit function from which the time constant could be extracted. Figure 10 shows an example of the filtered normal force experimental data and corresponding exponential curve fit during spark-in and spark-out from which the spark-in and spark-out time constants can be determined. In this example, the goodness-of-fit R^2 value was 0.995 indicating an excellent match between the exponential model and the experimental data. When the exponential curve fit was applied to the rest of the normal force experimental data, the resulting goodness-of-fit R^2 values were all above 0.969.

Figure 11 plots the resulting average spark-in and spark-out time constants (τ^{in} and τ^{out}) as a function of infeed rate for all the grinding experiments conducted in this research. The corresponding straight-line curve fit and error bars are

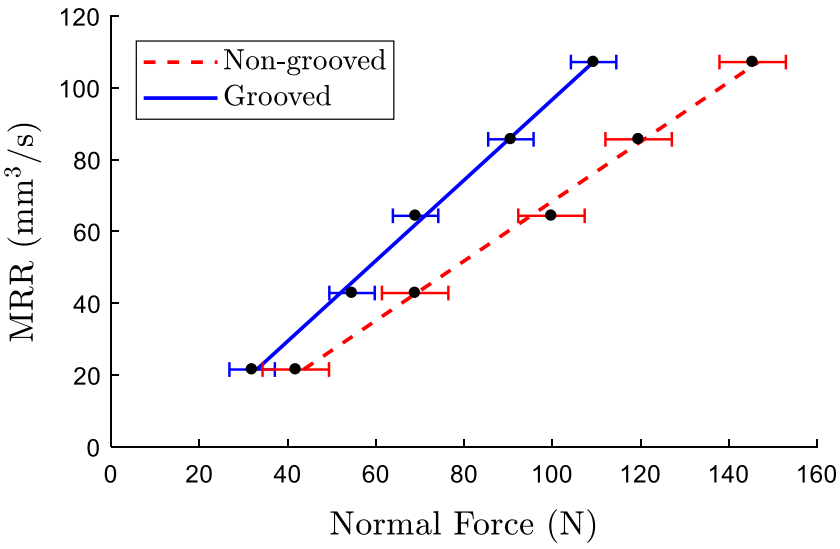

Fig. 7 MRR vs. normal force for cylindrical plunge grinding with grooved and non-grooved wheels

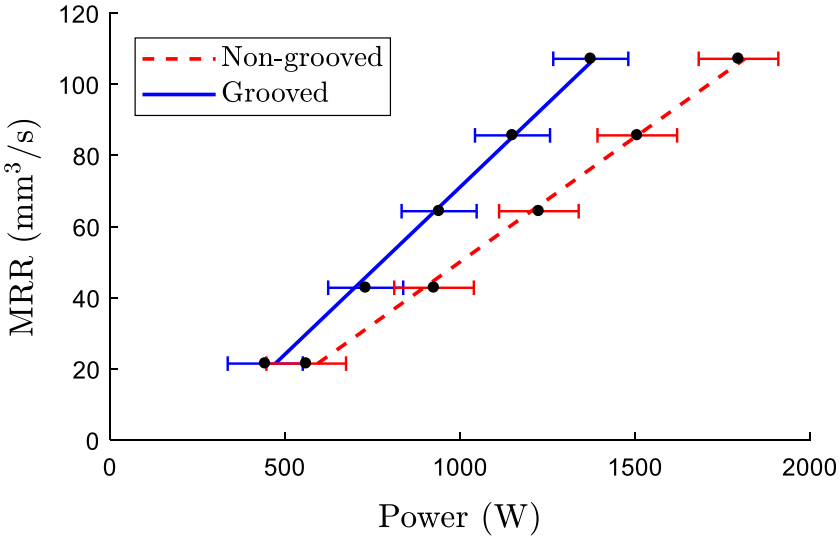

Fig. 8 MRR vs. spindle power for cylindrical plunge grinding with grooved and non-grooved wheels

superimposed for both the non-grooved and grooved wheels. The results show a slight decrease in the time constant for larger infeed rates for most cases, and there was, on average, a 21% decrease in the time constant when using a grooved grinding wheel. Cheng [18] indicates that the time constant τ is a measure of the effects of the overall grinding machine system stiffness, the grinding force coefficient which relates the normal force to the depth of cut, and the workpiece rotational speed. He then demonstrates how the time constant can be used in the following first-order model of material removal to describe the real grinding depth of cut as a function of time $r_w(t)$ for both the spark-in and spark-out phases:

$$\text{spark–in} \quad r_w(t) = v_f\left(t - \tau + \tau \cdot e^{-\frac{t}{\tau}}\right) \tag{4}$$

$$\text{spark–out} \quad r_w(t) = v_f\left(t_1 - \tau \cdot e^{-\frac{(t-t_1)}{\tau}}\right) \tag{5}$$

where v_f is the infeed rate and t_1 is the time at which dwell occurs and spark-out begins. The time constant for spark-in and spark-out are assumed to be the same in Eqs. (4) and (5). It can be seen from Fig. 11, however, that for the conditions used in this research, the time constants for spark-out were larger than the time constants for spark-in—over 50% larger on average.

To accommodate for the different spark-in and spark-out time constants τ^{in} and τ^{out}, the present authors modified Eqs. (4) and (5) as follows:

$$\text{spark–in} \quad r_w(t) = v_f\left(t - \tau^{in} + \tau^{in} \cdot e^{-\frac{t}{\tau^{in}}}\right) \tag{6}$$

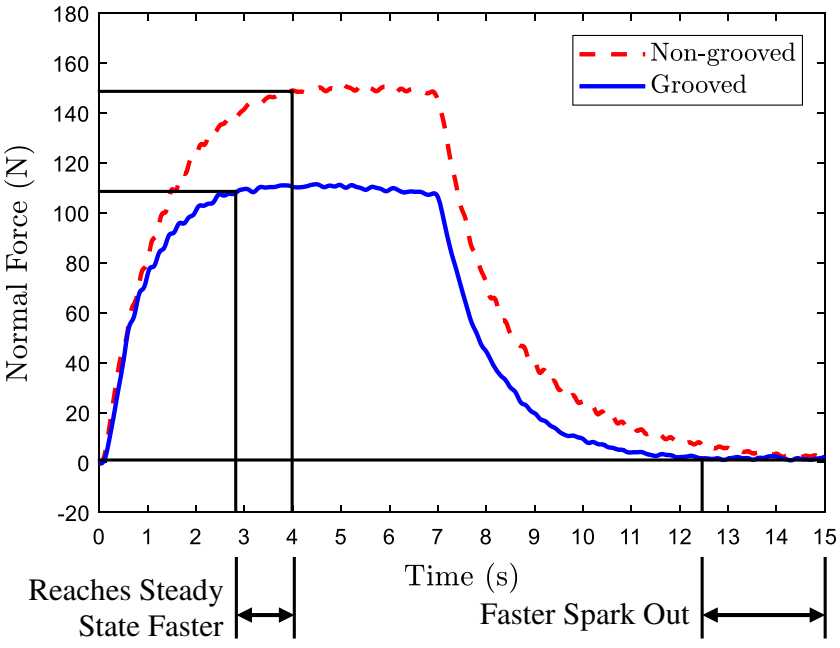

Fig. 9 Comparison of filtered normal force curves for non-grooved and grooved wheels

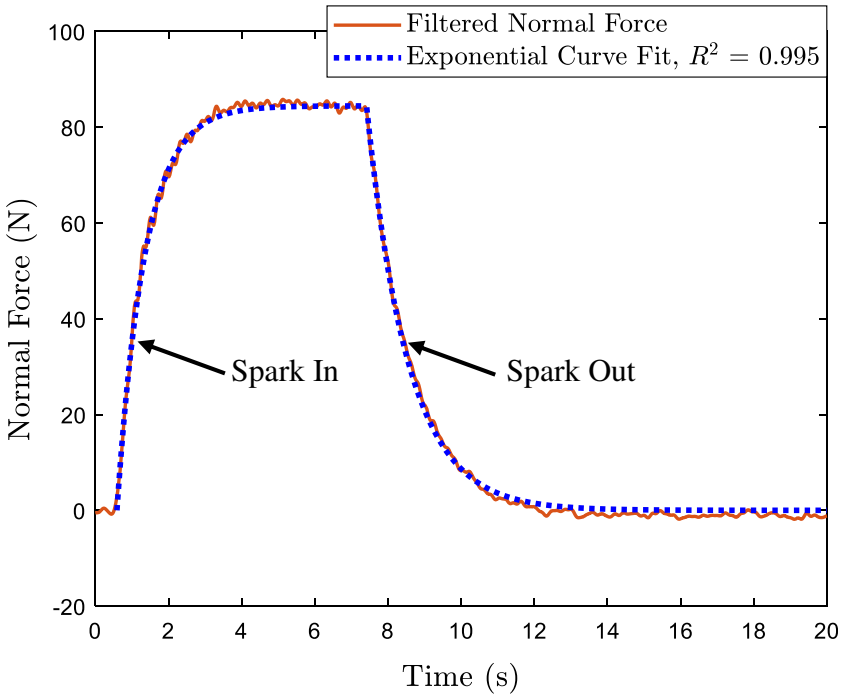

Fig. 10 Example exponential curve fitting of the filtered normal force

$$\text{spark-out} \quad r_w(t) = v_f\left(t_1 - \tau^{in}\cdot e^{-\frac{(t-t_1)}{\tau^{out}}}\right) \tag{7}$$

Having calculated the time constants from the experimental normal force data, we can use the models described by Eqs. (2) and (3) to simulate the normal force as well as Eqs. (6) and (7) to simulate the removal of workpiece material to study the cycle time of the plunge grinding operation for both non-grooved and grooved wheels. For example, referring to Fig. 4, grinding with a non-grooved wheel at an infeed rate of 1.02 μm/rev (the lowest infeed rate tested in Table 2) corresponds to a steady-state normal force of 44 N. Interpolating along the linear trend line for the grooved wheel in Fig. 4 shows that the grooved grinding wheel exhibits a steady-state normal force of 44 N at an infeed rate of 1.59 μm/rev. As a result, for the same steady-state normal force, it takes less time for the grooved grinding wheel to reach a specified depth of cut than the non-grooved wheel. Interpolating along the linear trend lines in Fig. 11 enables the corresponding spark-

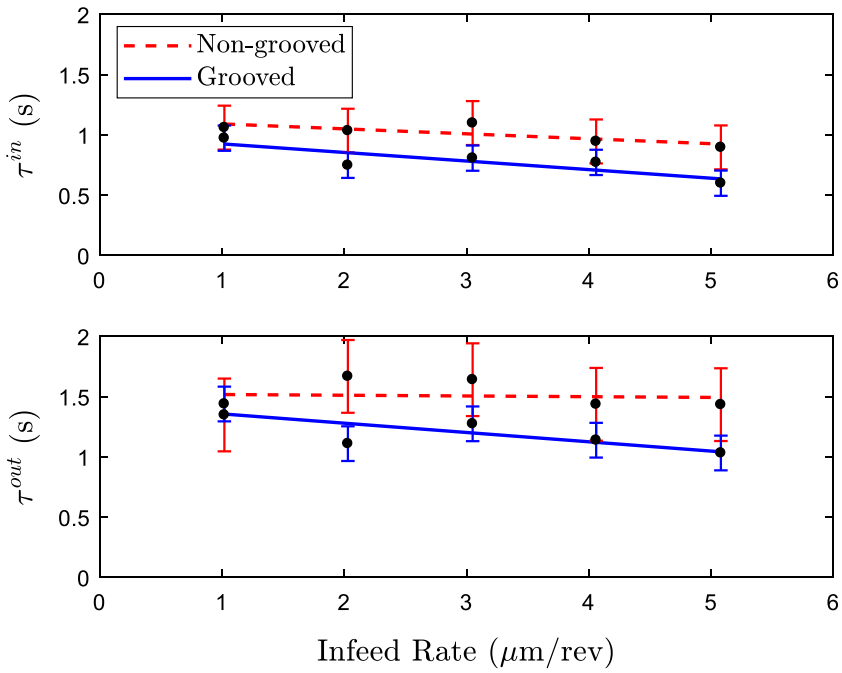

Fig. 11 Spark-in and spark-out time constants vs. infeed rate for cylindrical plunge grinding with groove and non-grooved wheels

in and spark-out time constants to be determined for the non-grooved wheel at an infeed rate of 1.02 μm/rev and the grooved wheel at an infeed rate of 1.59 μm/rev. Using these spark-in and spark-out time constants, the steady-state normal force of 44 N and a commanded depth of cut of 36 μm (from Table 2 for an infeed rate of 1.02 μm/rev), Fig. 12 plots the resulting simulated normal forces, commanded depths of cut, and simulated depths of cut for both the non-grooved and grooved wheels.

Figure 12a, b predicts that it would take (assuming three time constants to completely spark-out the workpiece) about 11.6 s for the non-grooved wheel to reach a commanded depth of cut of 36 μm with a normal force of 44 N. Figure 12a, c, however, predicts that (for the same normal force) it would only take about 8.5 s for the grooved wheel to reach the same commanded depth of cut of 36 μm—which corresponds to a 27% improvement in overall cycle time. A similar analysis was carried out for a normal force of 109 N in Fig. 4 which corresponds to a grooved wheel having an infeed rate of 5.08 μm/rev (the highest infeed rate tested in Table 2) and a non-grooved wheel having an infeed rate of 3.6 μm/rev (interpolating along the linear trend line). Corresponding time constants were interpolated from Fig. 11, and the resulting simulations for a commanded depth of cut of 178 μm (from Table 2 for an infeed rate of 5.08 μm/rev) are presented in Fig. 13. Referring to Fig. 13a, b, the models predict that it would take about 14.4 s for the non-grooved wheel to reach a commanded depth of cut of 178 μm with a normal force of about 109 N. Figure 13a, b, however, predicts that (for the same normal force) it would only take about 10.1 s for the grooved wheel to reach the same commanded depth of cut of 178 μm—which is a 30% improvement in overall cycle time. These results suggest that grooved grinding wheels have the potential to significantly improve the cylindrical grinding process.

The improvements in the time constants can be explained with the help of Fig. 14 which is based on Tlusty's [19] discussion of the effects of cutting forces on workpiece deflections. In the figure, the grinding wheel's infeed rate is a. The stiffness of the grinding machine, grinding wheel, rotary axis, and workpiece has been modeled as a single lumped parameter k_m. The normal force F_n can be related to the depth of cut using a cutting stiffness k_a which is proportional to the specific energy and the force ratio. In practice, one does not observe a linear relationship between normal force and depth of cut. More typical would be a monotonically increasing normal force with depth of cut; however, the authors feel that, for the purposes of explaining trends in the results, this assumption is reasonable. Since the machine stiffness and cutting stiffness are in series,

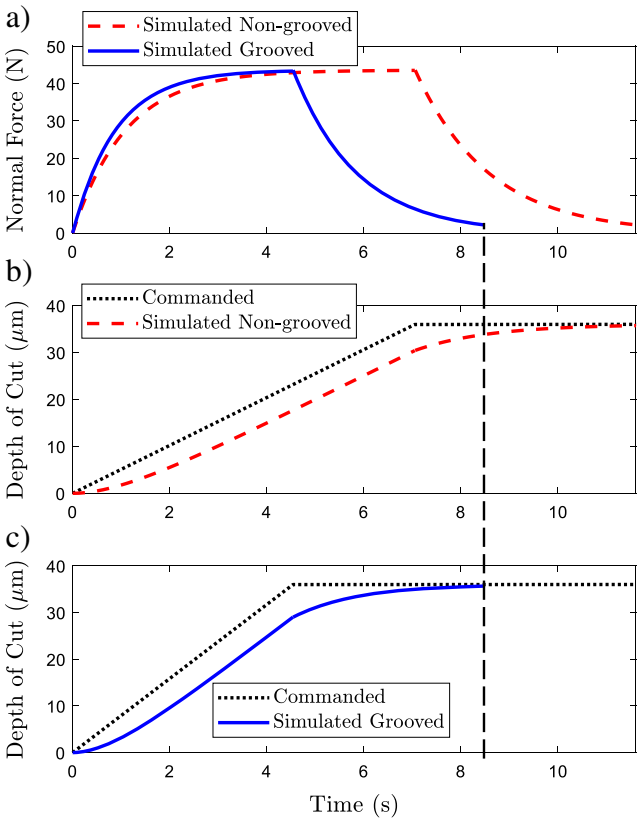

Fig. 12 Simulated normal forces and depths of cut for a 36 μm plunge using non-grooved and grooved wheels showing a 27% improvement in cycle time

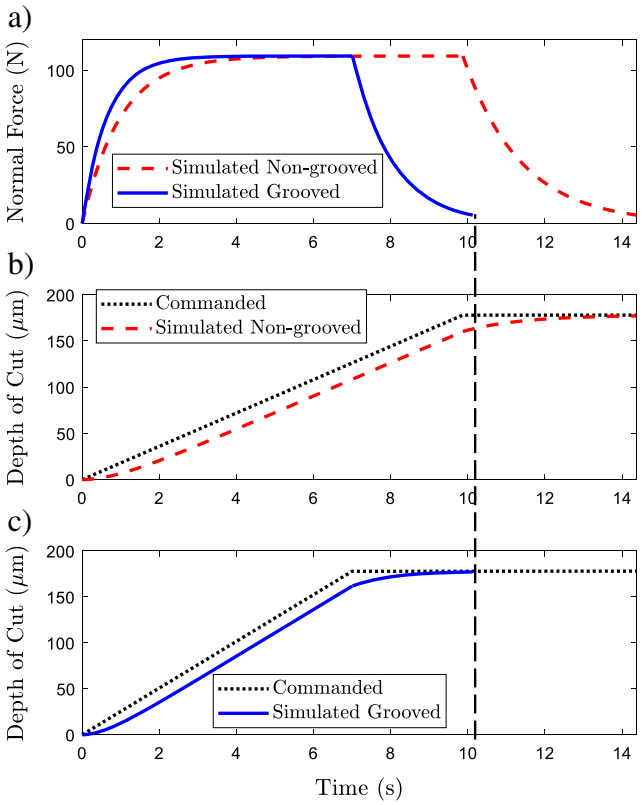

Fig. 13 Simulated normal forces and depths of cut for a 178 μm plunge using non-grooved and grooved wheels showing a 30% improvement in cycle time

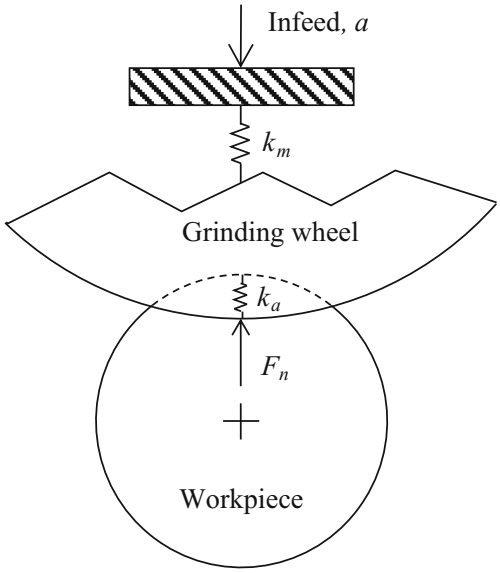

Fig. 14 Illustration of cutting stiffness and machine stiffness in cylindrical grinding

$$F_n = k_a a' = k_m x \tag{8}$$

where a' is the actual infeed rate and x is the infeed error per revolution caused by the machine deflection. The desired infeed a is then the sum of the actual infeed and the machine deflection:

$$a = a' + x \tag{9}$$

By rearranging Eq. (8) and substituting for a' in Eq. (9), the following relationship between the desired infeed and the infeed error per revolution can be deduced:

$$x = a\left(\frac{\frac{k_a}{k_m}}{1+\frac{k_a}{k_m}}\right) \tag{10}$$

From these equations, it is clear that a reduction in cutting stiffness caused by a reduction in specific energy obtained by grooving a wheel will result in a reduction in infeed error per revolution. Since the error per revolution is reduced, it is reasonable to assume that it will take fewer revolutions of the grinding wheel to eliminate this error resulting in a reduction in the time constant.

5 Conclusions

This work has shown that, for the conditions used in this research, there were significant benefits to using grooved grinding wheels in cylindrical grinding including a reduction of normal force by 36%, a reduction of tangential force by 32%, a reduction of spindle power by 29%, a reduction of specific energy by 28%, and a reduction of time constants by 21%. There was an increase in surface roughness of 38% with no effect on roundness. The reduction in time constants when using grooved wheels is particularly interesting because of its direct relation to improved grinding productivity. Simulations carried out using the identified models of the grinding system indicate that improvements in overall grinding cycle time of up to 30% may be achievable when using a grooved grinding wheel.

Acknowledgements The authors would like to acknowledge and thank the Natural Science and Engineering Research Council of Canada (NSERC) and the Nova Scotia Research and Innovation Graduate Scholarship (NSGS) for their financial support of this research.

References

1. Dong S, Danai K, Malkin S, Deshmukh A (2004) Continuous optimal infeed control for cylindrical plunge grinding, part 1: methodology. J Manuf Sci Eng Trans ASME 126(2):327–333
2. Li HN, Axinte D (2016) Textured grinding wheels: a review. Int J Mach Tools Manuf 109:8–35
3. Forbrigger C, Bauer R, Warkentin A (2017) A review of state-of-the-art vitrified bond grinding wheel grooving processes. Int J Adv Manuf Technol 90(5–8):2207–2216
4. Nakayama K, Takagi J, Abe T (1977) Grinding wheel with helical grooves - an attempt to improve the grinding performance. Ann CIRP 26(1–2):133–138
5. J. Verkerk, "Slotted wheels to avoid cracks in precision grinding," in *Proc - Annu Abrasive Eng Soc Conf/Exhib, 17th*, Pittsburgh, PA, 1979
6. de Oliveira JF, Bottene AC, França TV (2010) A novel dressing technique for texturing of ground surfaces. CIRP Ann Manuf Technol 59(1):361–364
7. da Silva EJ, de Oliveira JF, Salles BB, Cardoso RS, Reis VR (2013) Strategies for production of parts textured by grinding using patterned wheels. CIRP Ann Manuf Technol 62(1):355–358
8. Uhlmann E, Hochschild L (2013) Tool optimization for high speed grinding. Prod Eng 7(2–3):185–193
9. Mohamed A-MO, Bauer R, Warkentin A (2013) Application of shallow circumferential grooved wheels to creep-feed grinding. J Mater Process Technol 213(5):700–706
10. Choi TJ, Subrahmanya N, Shin YC (2008) Generalized practical models of cylindrical plunge grinding processes. Int J Mach Tools Manuf 48(1):61–72
11. Drew SJ, Mannan MA, Ong KL, Stone BJ (2001) The measurement of forces in grinding in the presence of vibration. Int J Mach Tools Manuf 41(4):509–520
12. Mohamed A-MO, Bauer R, Warkentin A (2014) A novel method for grooving and re-grooving aluminum oxide grinding wheels. Int J Adv Manuf Technol 73(5–8):715–725
13. Mohamed A-MO, Bauer R, Warkentin A (2016) Uncut chip thickness and coolant delivery effects on the performance of circumferentially grooved grinding wheels. Int J Adv Manuf Technol 85(5–8):1429–1438
14. S. Malkin and C. Gao, Grinding technology: theory and applications of machining with abrasives, 2nd edition, Industrial Press, 2008
15. J. R. Davis and et al., ASME handbook, volume 16 machining, OH: ASM International, Metals Park, 1999

16. S. Malkin and Y. Koren, "Optimal infeed control for accelerated spark-out in plunge grinding," in *Am Sco Mech Eng Pap*, New York, 1984
17. Jiang C, Guo DB, Li HL (2013) Estimation of the time constant of precision plunge grinding in dwell period based on acoustic emission measurement. Adv Mater Res 690 693:3262–3265
18. K. Cheng, Machining dynamics fundamentals, applications and practices, Springer, 2009
19. G. Tlusty, Manufacturing processes and equipment, **Prentice Hall**, 2000